Density Functional Theory Simulation of Cobalt Oxide Aggregation and Facile Synthesis of Cobalt oxide, Gold and Multiwalled Carbon Nanotubes Ternary Composite for a High Performance Supercapattery

Javed Iqbal[1,2], Lijie Li[3], Arshid Numan[4#], Saqib Rafique[3], Rashida Jafer[5], Sharifah Mohamad[1], Mohammad Khalid[4], K. Ramesh[6], S. Ramesh[6*]

[1]*Department of Chemistry, Faculty of Science, University of Malaya, Kuala Lumpur 50603, Malaysia.*

[2]*Center of Nanotechnology, King Abdulaziz University, Jeddah 21589, Saudi Arabia.*

[3]*Multidisciplinary Nanotechnology Centre, College of Engineering, Swansea University, Swansea SA1 8EN, United Kingdom.*

[4]*Graphene & Advanced 2D Materials Research Group (GAMRG), School of Science and Technology, Sunway University, No. 5, Jalan Universiti, Bandar Sunway, 47500 Subang Jaya, Selangor, Malaysia.*

[5]*Department of Physics, Faculty of Science, King Abdulaziz University, Jeddah 21589, Saudi Arabia.*

[5]*Center for Ionics University of Malaya, Department of Physics, Faculty of Science, University of Malaya, Kuala Lumpur 50603, Malaysia.*

*Corresponding authors

[*] E-mail: rameshtsubra@gmail.com,

numan.arshed@gmail.com

Tel: +603-7967 4391, Fax: +603-7967 4146

ABSTRACT

A novel ternary composite consisting of cobalt oxide (Co_3O_4) nanoparticles (NPs) grown on multiwalled carbon nanotubes (MWCNTs) and mixed with gold (Au) NPs is synthesized by single step hydrothermal route. Initially, density functional theory (DFT) simulation was carried out to model the aggregation of Co_3O_4 NPs and validated further with the experimental results. To circumvent this issue, MWCNTs with gold NPs were introduced which significantly reduced the particle aggregations. The standard three electrodes cell studies revealed that Co_3O_4/Au@MWCNTs composite possesses an excellent energy density, rate capability and very good cyclic stability compared to unsupported Co_3O_4 or the binary Co_3O_4@MWCNTs. The promising electrochemical performance compared to the single Co_3O_4 or the binary Co_3O_4@MWCNTs materials is assigned to the synergetic effects of MWCNTs and Au to disaggregate the Co_3O_4 NPs and to enhance the overall conductivity, respectively. In order to get insight, the evaluation performance, the two electrodes devices were assembled employing activated carbon as a negative electrode and Co_3O_4/Au@MWCNTs composite as a positive electrode material. The two electrodes supercapattery device demonstrated splendid cycling stability with a retention value of 91.70 % in 1 M KOH for over 3500 cycles. Additionally, it exhibited excellent energy density of 18.80 Wh Kg^{-1} at a power density of 302.00 W Kg^{-1}. These encouraging outcomes can be associated to the distinctive morphology, outstanding conductive networks, increased electroactive sites, and emergence of strong networking of Co_3O_4, MWCNT and Au in the ternary composite.

Keywords: Co_3O_4 aggregation, Co_3O_4/Au@MWCNTs composite, DFT simulations, supercapattery, energy storage.

1. INTRODUCTION

The rapid emergence of miniaturized electronics requires widespread and concerted research efforts into the higher energy density storage devices, also called supercapacitors.[1, 2, 3] Supercapacitors are currently acknowledged as the basic building-blocks of future integrated power sources because of their promising power density, essentially rapid charge/discharge cycles, outstanding low temperature performance and ecofriendly features.[4, 5] Their unique characteristics have expanded their scope ranging from modern recreational facilities such as wearable electronics to smart building windows, non-planar translucent tops and the automobile windshields *etc.*[6, 7] Basically, a supercapacitor comprises of two highly conductive electrodes separated by mobile ionic species within an electrolyte.[8] Contrary to conventional capacitors, the charge is balanced by the adsorption of cations and anions at the electrodes surface upon applying the voltage, and the outstanding efficiency of supercapacitors is attributed to the highly reversible ion adsorption mechanism. Therefore, for the realization of highly efficient devices, the electrode materials and design configuration should potentially possess excellent electrochemical and optoelectronic performance.[9,10]

Unlike the batteries, the charging is not confined by the diffusion of ions in the bulk of the electrodes in the supercapacitors. Therefore, they possess higher power densities that can complement and sometimes completely replace the batteries when higher power delivery or uptake is desired. [11] However, the lesser energy density of supercapacitors compared to the conventional batteries is still a bottleneck in their realization for various applications.[12] It is highly desired to enhance the energy density of supercapacitors while maintaining their power density. In recent years, a new approach employing synergistic hybridization of both the supercapacitors and

batteries has been developed for the realization of the so-called supercapattery that compliments the distinguished features of both the devices.[13] The supercapattery (asymmetric supercapacitor or hybrid supercapacitor are wrongly used terms), is a synergistic hybridization of the eminent energy-storage features of the batteries by employing pseudoactive battery grade materials as a positive electrode and escalated power density features of a capacitor while employing carbonaceous materials as a negative electrode.[14] Therefore, the realization of high performance supercapattery clearly demands the exploitation of new material combinations/compositions and design configurations. It is noteworthy that the current work demonstrates the utilization of novel materials combination in the supercapattery electrode, therefore, the device will be termed as supercapattery hereafter, throughout the article to avoid any confusion due to its similarity with the supercapacitor.

The key factors for the supercapattery to achieve the excellent energy density and overall high performance is the selection of optimized electrode material composition/combination and design configuration.[15] In this context, transition metal oxides including NiO, MnO_2, V_2O_5, MoO_2, Fe_2O_3 and Co_3O_4, *etc.* have been employed as an positive electrode materials in high performance energy storage devices over the recent years.[16, 17] Among the transition metal oxides, Co_3O_4 is the most investigated electrode material due to its controllable nanostructures, its abundance in nature, ecofriendly properties and its ultra-high theoretical specific capacitance (3560 F/g).[4, 18] The diverse polar sites in the Co_3O_4 crystals are achieved via the distribution of its bivalent state (Co^{2+}) over the tetrahedral and trivalent state (Co^{3+}) over the octahedral sites. In addition, these oxidation states enable the structure to achieve the features of high catalytic activity and high surface to volume ratio that ultimately lower the recombination of charges and facilitate the rapid charge transport mechanism on the electrode.[19] Despite the fact that Co_3O_4 possesses several advantages as a stand-

alone electrode material, it still lacks in many aspects. Firstly, aggregation of Co_3O_4 nanoparticles (NPs) causes a considerable reduction in their active sites that ultimately induces quick capacity retention and morphological disorder in the course of the charge-discharge cycle.[20] Secondly, the breakage and even crumbling of Co_3O_4 based electrodes originating from the major volume variation during the cycling process ultimately lead to the capacity reduction.[21] Therefore, much devotions have been given to blend Co_3O_4 with other materials. Thus, synergistic hybridization of Co_3O_4 with the multiwalled carbon nanotubes (MWCNTs) to reduce the aggregation of Co_3O_4 along with the highly conductive gold (Au) NPs using simple and cost-effective approach is particularly attractive to address the aforementioned issues and to uplift the overall efficiency of the supercapattery.[22]

The present work simulates the Co_3O_4 aggregation phenomenon using first principle method by Density Functional Theory (DFT) modeling. Further to circumvent the issues associated with Co_3O_4 as stand-alone material, it reports a facile, cost effective and single-step hydrothermal process to synthesize Co_3O_4/Au@MWCNTs ternary composite as an electrode material in supercapattery devices. Carbonaceous materials such as MWCNTs improve the cycling stability and enhance the electrochemical active sites by facilitating charge transfer and significantly reducing the aggregation of NPs.[13, 23] The Co^{2+} and Co^{3+} oxidation states of Co_3O_4 are reactive towards the sp^2 hybridized carbon atoms of MWCNTs. Therefore, when the sidewalls of MWCNTs react with the cobalt ions, it results in the grafting of Co_3O_4 NPs onto the MWCNTs.[24] In addition, the MWCNTs are exceedingly narrow conductors and their diameters are several atomic lengths only. They possess hollow structure, high porosity and ballistic electron transport. Therefore, MWCNTs provide an ideal platform to reduce the aggregation of Co_3O_4 nanoparticles and facilitate the movement of electrons for the metal oxide when synthesized on

the MWCNTs matrix, primarily in the EC applications. Thus, the growth of Co_3O_4 NPs onto the MWCNTs matrix will not only reduce the clustering of Co_3O_4 but also prevents structural disorder and capacity fading.[25] In addition, the high band gap of metal oxides induces the slower electron transfer, therefore, noble metals such as Au in the Co_3O_4/Au@MWCNTs ternary composite can significantly enhance the conductivity through the wider electron transfer channels. These features will ultimately contribute to the redox reaction. The electrochemical performance of ternary composite, Co_3O_4/Au@MWCNTs was evaluated and finally tested systematically for the supercapattery applications as a positive electrode material. The synthesized material showed significant performance including superior specific capacity, high rate capability and enhanced cycling stability compared to single Co_3O_4 and binary Co_3O_4@MWCNTs as reference materials in addition to the already reported results.

2. EXPERIMENTAL SECTION

2.1 Materials

MWCNTs were supplied by Beytube, Germany. Activated carbon (AC), cobalt chloride hexahydrate ($CoCl_2.6H_2O$), poly (vinylidene fluoride) and acetylene black were obtained from Sigma-Aldrich. Hydrochloric acid (35%), ammonia solution (28%) and 1-Methyl-2-pyrrolidinone (99.5%) were obtained from Merck. Auric chloride precursor was obtained from ABCR GmbH & CO. KG. In addition, all solutions were prepared in deionized (DI) water.

2.2 Preparation of Co_3O_4/Au@MWCNTs composite

MWCNTs were acid-treated to improve their aqueous dispersion by introducing the electronegative functional groups. Moreover, this process eliminates the metal and carbon residues, also introduce porosity and increases the surface area.[26] In this context, MWCNTs were

treated with acid following our previously reported method.[13] Further, 1mM of the $CoCl_2.6H_2O$ dissolved in 20 mL of DI water followed by drop-wise addition of 15 mL of NH_4OH (6%) at the rate of 1 mL min^{-1} under constant stirring for one hour. With respect to cobalt precursor, 5 wt. % of $AuCl_3$ was dissolved in 5 mL of DI water and added drop-wise into the above mixture while stirring for further 30 min followed by the addition of 16 wt. % of MWCNTs (with respect to cobalt precursor) dispersed in 10 mL of DI water. Finally, the Teflon lined stainless steel autoclave was used to carry out the hydrothermal reaction by keeping the resultant mixture (50 mL) at 150 °C for 5h. The precipitates were washed by centrifugation with excessive DI water and ethanol followed by drying in an oven (60 °C). The same protocol was replicated to synthesize Co_3O_4 NPs without MWCNTs and Au-precursor. Also, Co_3O_4@MWCNTs binary composite was synthesized by employing the same procedure without Au-precursor.

2.3 Material characterization

The density functional theory calculations on Co_3O_4 nanoparticles have been performed using the commercial software – Quantum ATK from Synopsys Inc. We built the molecular models for Co_3O_4 nanoparticles with various radiuses. Geometrical optimization and total energy analysis have been subsequently conducted. Detailed simulation parameters and results are presented in the result section. The micro-morphology, mapping and elemental composition were characterized using field emission scanning electron microscopy (FE-SEM) JSM-7600F microscope (JEOL, Japan) and energy dispersive spectroscopy (EDS). The crystal structure and phase identification of the Co_3O_4/Au@MWCNTs composite were carried out in 2θ scanning range of 10° to 70° using a Philips X'pert X-ray diffractometer (XRD) equipped with Cu-Kα source (λ = 1.5418 A°). X-ray photoelectron spectroscopy (XPS) was performed on a PHI 5000 Versa Probe Scanning ESCA Microprobe (PHI 5000 Versa Probe II, USA) in an ultrahigh vacuum chamber

(~10^{-10} m bar) using monochromatic Al-Kα (hν=1486.6 eV) anode. Deconvolution of each spectrum by curve fitting of XPS core-level spectra was done using Multipack software (version 9, ULVAC-PHI, Inc.).

2.4 Electrode fabrication and electrochemical measurements

The supercapattery devices were fabricated using the Co_3O_4/Au@MWCNTs ternary composite as a positive electrode and AC as a negative electrode material. Briefly, 75 wt. % of Co_3O_4/Au@MWCNTs, 15 wt. % of AC and 10 wt. % of PVdF were blended in NMP and stirred for 12 hours to obtain a homogeneous slurry. The resultant paste was coated onto the nickel foam (1×1 cm^2), followed by drying in an oven at 90 °C for 12 h. The mass loading of the synthesized redox active material was about 5.00±0.05 mg. The electrochemical (EC) measurements were carried out in 1 M KOH electrolyte at room temperature. Cyclic voltammetry (CV), galvanostatic-charge discharge (GCD) and electrochemical impedance spectroscopy (EIS) measurements were performed using a potentiostat (Gamry Interface 1000 Instrument, USA) electrochemical work station. For the performance comparison of Co_3O_4/Au@MWCNTs ternary composite, both the individual Co_3O_4 NPs and the Co_3O_4@MWCNTs binary composite were also characterized by following the same measurement steps as described for the ternary blend.

3. RESULTS AND DISCUSSION

Figure 1 illustrates a schematic diagram of the current work exhibiting DFT simulation of Co_3O_4 NPs, preparation of the Co_3O_4/Au@MWCNTs ternary composite and its subsequent utilization as a positive electrode material in the supercapattery. The synergy of eminent power delivery characteristics of capacitors and prominent energy-storage features of batteries in one device, the so-called supercapattery is actually the combination of battery and capacitor features

together that makes it a novel device which stores energy by a dual mechanism.[27] To investigate the aggregation issue associated with the Co_3O_4 NPs, first principle method has been used to perform DFT simulation of Co_3O_4 NPs. The model qualitatively analyzes the aggregation of Co_3O_4 NPs. Further, the effects of MWCNTs to mitigate the Co_3O_4 aggregation, and Au to enhance the conductivity in the Co_3O_4/Au@MWCNTs composite have been thoroughly explored. The complete experimental details can be found in the Experimental Section.

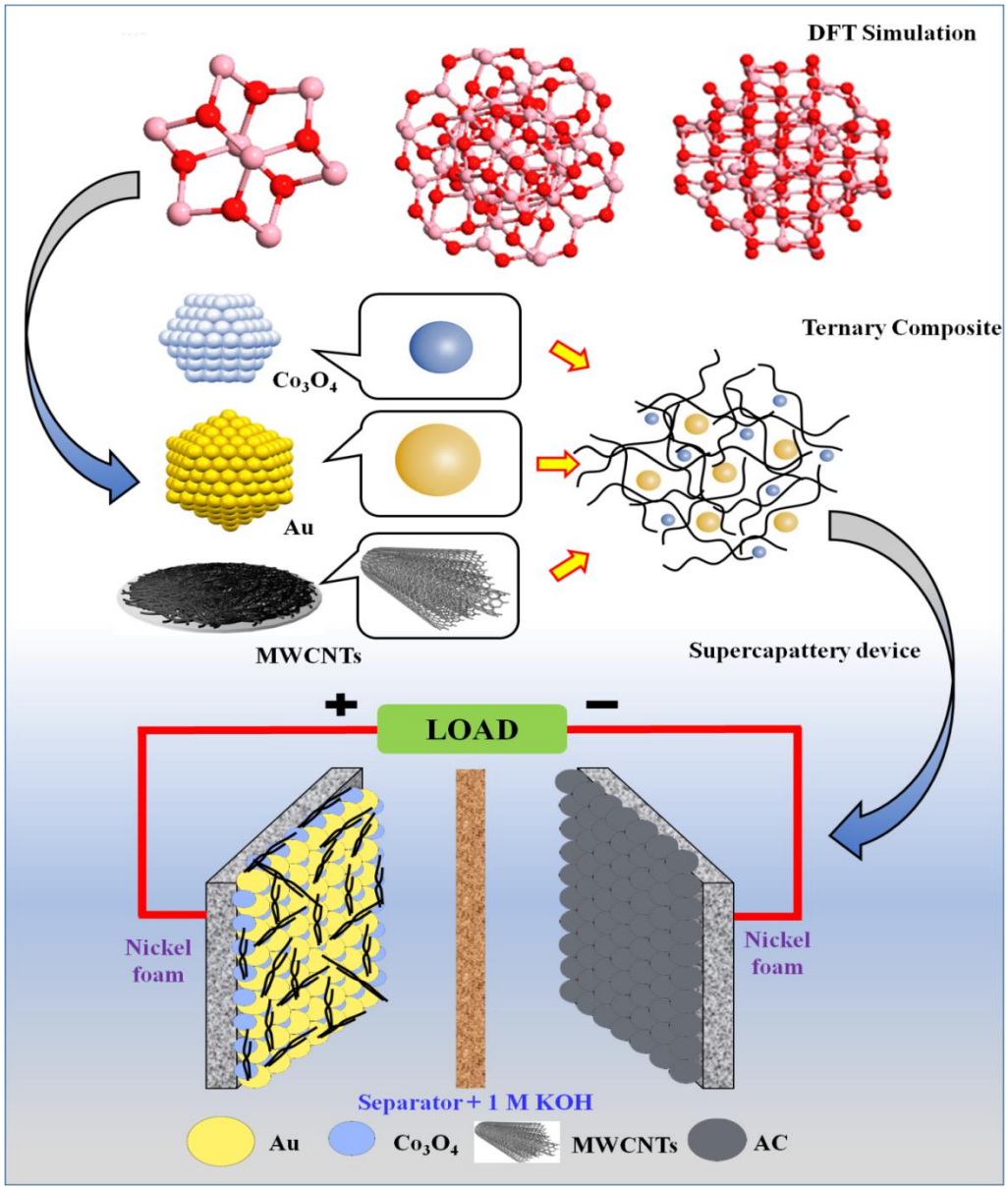

Figure 1: Schematic illustration of DFT simulation of Co_3O_4 NPs aggregation (top), preparation of Co_3O_4/Au@MWCNTs ternary composite (middle) and supercapattery employing Co_3O_4/Au@MWCNTs ternary composite as a positive electrode material (bottom).

3.1 DFT Modeling of Co_3O_4 Nanoparticles

First principle method was used to simulate the Co_3O_4 NPs. Particles with various sizes have been modeled and shown in **Figure 2**. The corresponding sizes and numbers of atoms are detailed in the figure caption. The first step of modeling was to optimize the particle geometry with the maximum force tolerance less than 0.05 eV/Å using the density functional theory (DFT) LCAO (linear combination of atomic orbitals) calculations. Several analyses based on the geometrically optimized particle have been performed including the total energy and projected density of states. According to the DFT, the total energy $E_T(n)$ is the free energy given by $E_T(n) = T(n) + E^{XC}(n) + E^{H}(n) + E^{ext}(n) - \sigma S$, where n is the electron density. The first term on the right side represents the kinetic energy, second denotes the exchange-correlation energy, the 3rd item includes all the electrostatic terms, fourth is the interaction energy with an external field, and the last one is the entropy contribution due to smearing of the occupation function. The total energy and its constituent energy items of Co_3O_4 particles with all the five sizes are shown in **Figure 3**. The external filed energy is zero and entropy-term is very small (< 1 eV) compared with the other three energy terms, which are not shown in **Figure 3**. As commonly defined, the "0" total free energy is for the case where all the atoms are infinitely separated and there is no movement. Hence, the total energy is negative, a smaller value of total energy indicates a higher level of NP stability. The trend demonstrated in **Figure 3** tells that stability increases with the increasing NPs size. It is reasonable to qualitatively deduce that the aggregation problem of the Co_3O_4 is attributed to the fact that smaller size NPs tend to join together to form a larger size NP with much more stability.

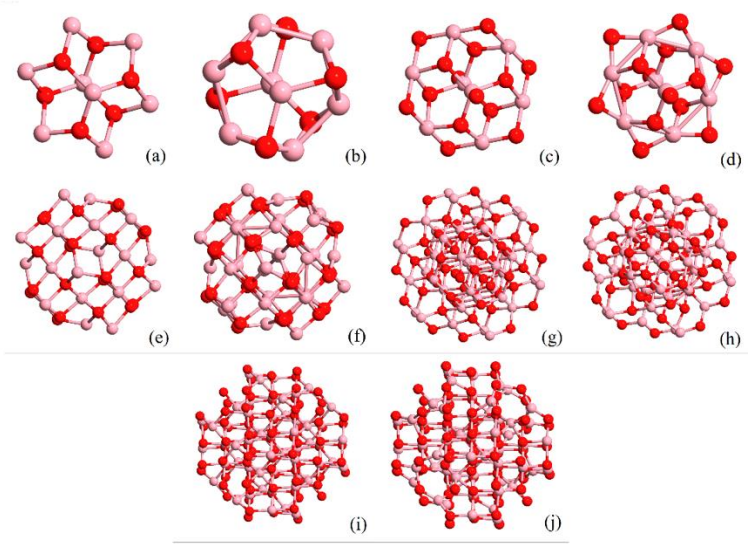

Figure 2: Atomic structure of Co_3O_4 NPs with different radiuses. **(a)** un-optimized structure with radius of 3 Å, total 14 atoms, **(b)** optimized 3Å NP, **(c)** un-optimized NP with 4Å radius, total 22 atoms, **(d)** optimized 4Å NP, **(e)** un-optimized 5Å NP, total 70 atoms, **(f)** optimized 5Å NP, **(g)** un-optimized 6Å NP, total 100 atoms, **(h)** optimized 6 Å NP, **(i)** un-optimized NP with 7Å radius, 148 atoms and **(j)** optimized 7Å NP.

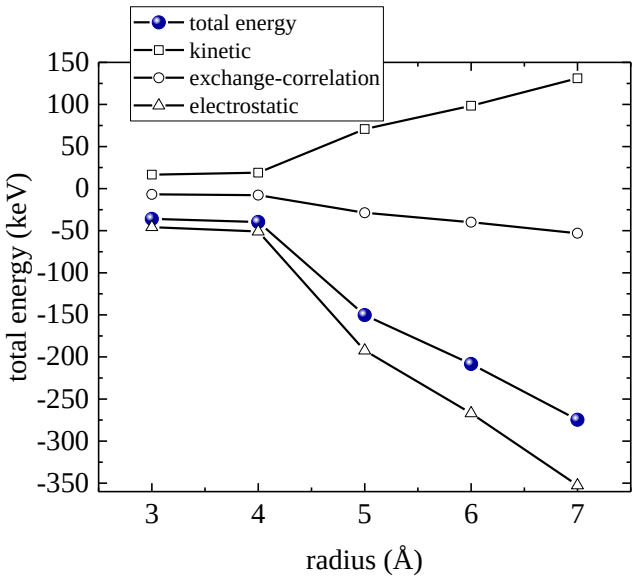

Figure 3: Calculated total free energy and its constituents (kinetic, exchange-correlation, electrostatic) of the Co_3O_4 NPs with different radiuses.

Figure 4 shows the simulated electron density of state (DOS) for five different sizes with radius incrementing from 3 Å to 7 Å. In general, it is seen that the electron density of the O element is greater than that of Co element for lower energies, and the DOS of Co is higher under high electron energies. Although the peak DOS reduces a little from 3Å NP to 4Å NP, the absolute value of the DOS follows an approximate increasing trend as the increase of the NP radius. Larger DOS resembles that of bulk materials.

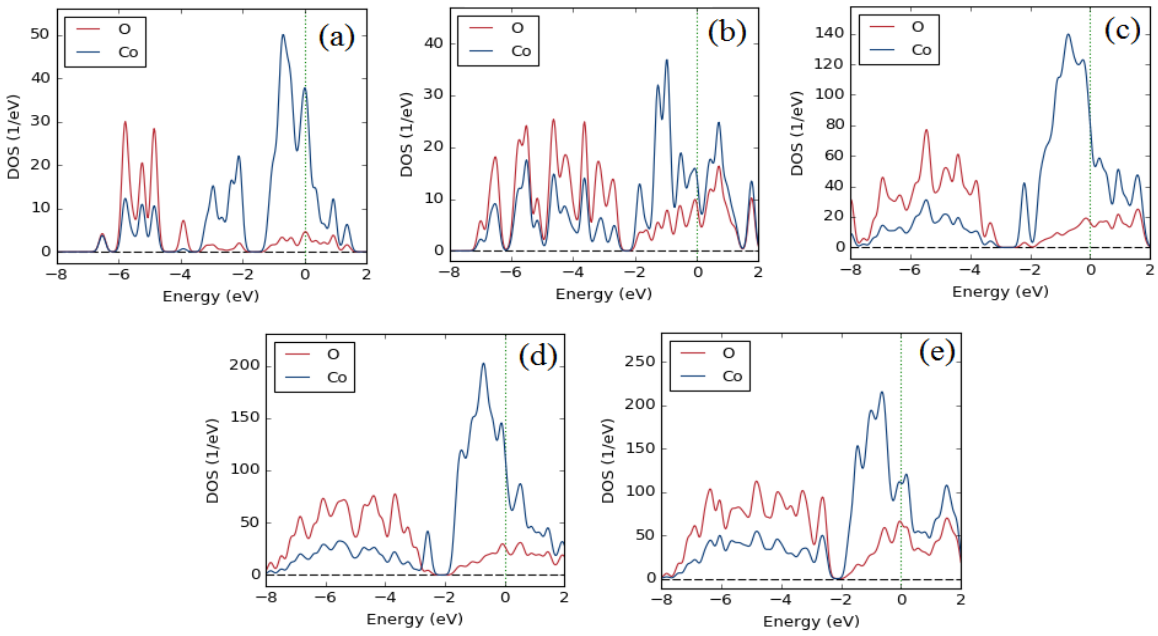

Figure 4: Calculated density of states for five Co_3O_4 NPs with different sizes. **(a)** 14 atoms, **(b)** 22 atoms, **(c)** 70 atoms, **(d)** 100 atoms and **(e)** 148 atoms.

3.2 Material Characterization of Co_3O_4/Au@MWCNTs ternary composite

The DFT simulation reported in **Section 3.1** confirms the aggregation of Co_3O_4 NPs as a stand-alone material that ultimately reduces their redox active sites and induces rapid capacity

fading. The Co_3O_4/Au@MWCNTs ternary composite has been synthesized to overcome stability issues associated with the single Co_3O_4 NPs as an electrode martial. The material is expected to bring a synergy of the high conductivity of Au NPs and ability of MWCNTs to disaggregate the Co_3O_4 NPs, hence the benefit of Co_3O_4/Au@MWCNTs ternary composite is two-folds. Therefore, the ternary composite and its individual content have been investigated for their morphological, compositional, structural and chemical properties.

3.2.1 Morphological Characteristics

FESEM is a valuable technique to characterize the morphology and microstructure of the prepared materials. The morphology of the Co_3O_4, its Co_3O_4@MWCNTs binary and Co_3O_4/Au@MWCNTs ternary composite are first studied by FESEM at different magnifications, as shown in **Figure 5**. The Co_3O_4 micrograph (**Figure 5a**) shows a granular structure with highly aggregated grains of 20-30 nm in size, directing to inadequate vulnerability of their cubic faces. Nevertheless, the aggregation is significantly reduced after introduction of MWCNTs in the Co_3O_4@MWCNTs binary composite shown in **Figure 5b**. The Co_3O_4 NPs were uniformly grown by a hydrothermal technique at oxygen containing functional groups on the MWCNTs matrix. **Figure 5c and 5d** represent the FESEM micrographs Co_3O_4/Au@MWCNTs ternary composite at a different resolution to illustrate the disaggregation of nanoparticles over the MWCNTs matrix. The ultra-small Au NPs on Co_3O_4 and MWCNTs are uniformly decorated on MWCNTs and Co_3O_4. The images also indicate the successful integration of Co_3O_4 and Au NPs onto the MWCNTs matrix.

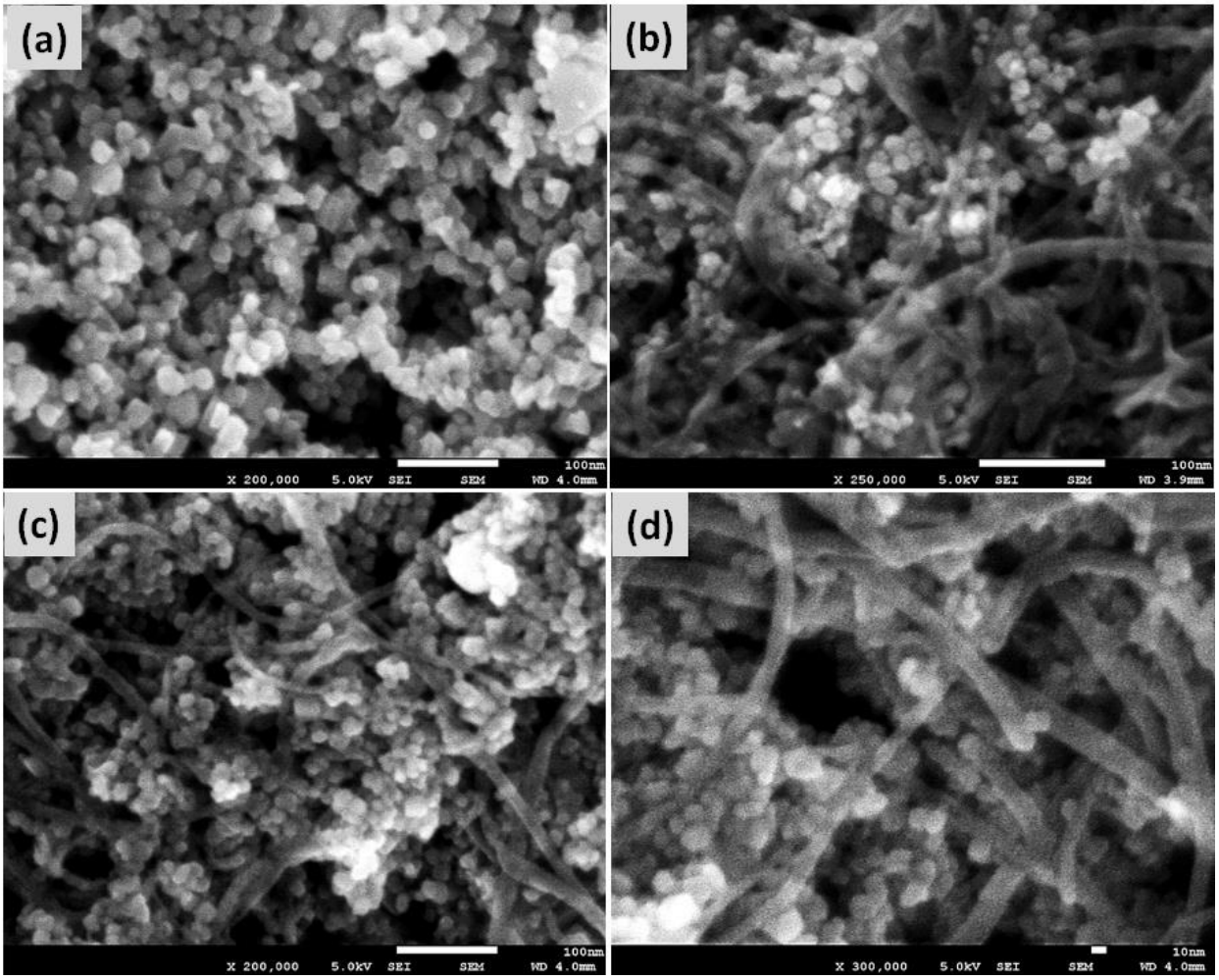

Figure 5: FESEM images of **(a)** Co_3O_4 NPs, **(b)** Co_3O_4@MWCNTs binary composite; **(c)** low and **(d)** high magnification images of Co_3O_4/Au@MWCNTs sample showing Co_3O_4 and Au NPs decorated on MWCNTs network.

Figure 6 depicts the constituent elements spectra and their corresponding EDS-mapping in the Co_3O_4/Au@MWCNTs ternary composite. The composite was characterized by selecting random areas using EDS analysis. The carbon is attributed to the MWCNTs, Co indicates the Co_3O_4 and Au peak indicates the presence of Au NPs. This confirms the successful emergence of Co_3O_4/Au@MWCNTs ternary composite. Moreover, the image mapping with distinguished colors

indicates the even distribution of all the individual constituents of the ternary composite across the matrix presented in **Figure 6a to e**. Particularly, **Figure 6f** verifies the even distribution of both the Co_3O_4 and Au on the MWCNTs network.

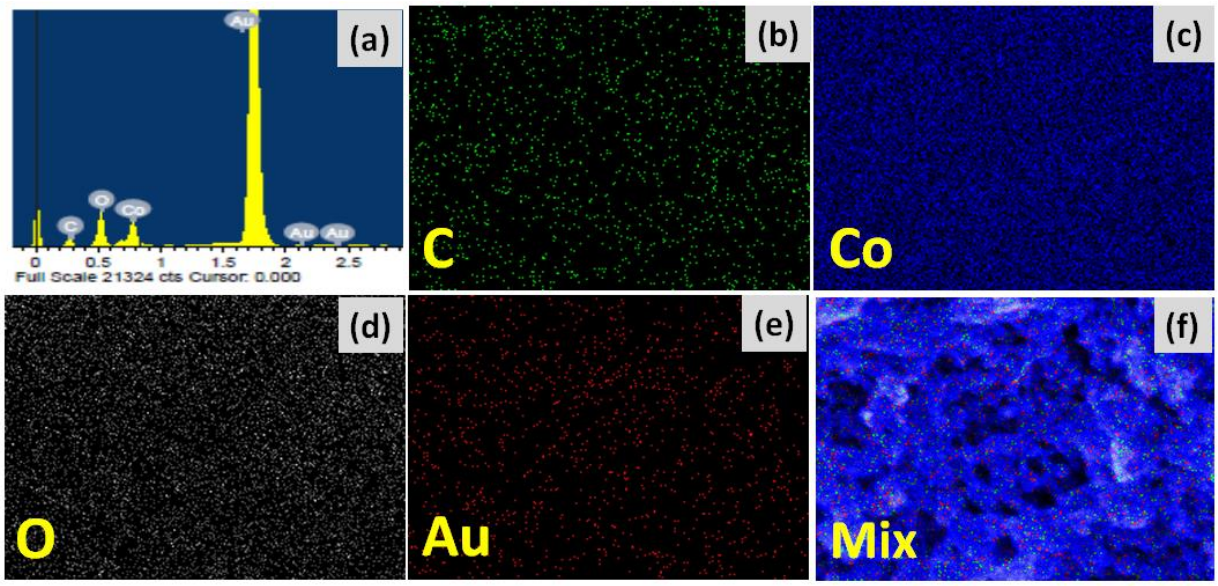

Figure 6: (a) EDS spectrum shows the elemental composition and, EDS-elemental mapping of **(b)** C, **(c)** Co, **(d)** O, **(e)** Au content of the Co_3O_4/Au@MWCNTs ternary composite. **(f)** Mix-verifies the even distribution of both the Co_3O_4 and Au NPs on the MWCNTs network.

3.2.2 Structural analysis

XRD patterns were recorded for the Co_3O_4 as well as its Co_3O_4@MWCNTs and Co_3O_4/Au@MWCNTs composites, as shown in **Figure 7**. The XRD patterns of Co_3O_4 and its composites showed intense reflections with sharp peaks, indicating the high crystallinity of the prepared material. XRD spectrum of Co_3O_4 exhibits characteristics peaks at 2θ value of 18.82°, 31°, 36.47°, 44.35°, 58.73° and 64.52°, which are ascribed to (111), (220), (311), (400), (511) and (440) lattice plans of cubic symmetry of Co_3O_4 crystal structure (space group: FD-3m(227)).

All the peaks are well indexed with the ICDD-PDF-00-009-0418 card number. The peak intensities considerably reduced in Co_3O_4@MWCNTs and Co_3O_4/Au@MWCNTs composites due to the fact that MWCNTs probably have partially covered the Co_3O_4 NPs. This indicates the successful integration of MWCNTs and Co_3O_4 in the binary matrix. The characteristic peaks of Au ascribed to (111), (200) and (220) at 38.10°, 44.37° and 65° respectively, in the Co_3O_4/Au@MWCNTs are corresponding to the cubic structure of Au and well indexed with the ICDD-PDF-00-002-1095 card number. The successful integration of MWCNTs and Au NPs to form a ternary composite has been confirmed by SEM-scanning and EDS mapping too. It is expected that inclusion of Au NPs may increase the conductivity by facilitating with the transfer channel which could eventually improve the EC functioning of the as synthesized ternary composite.[13]

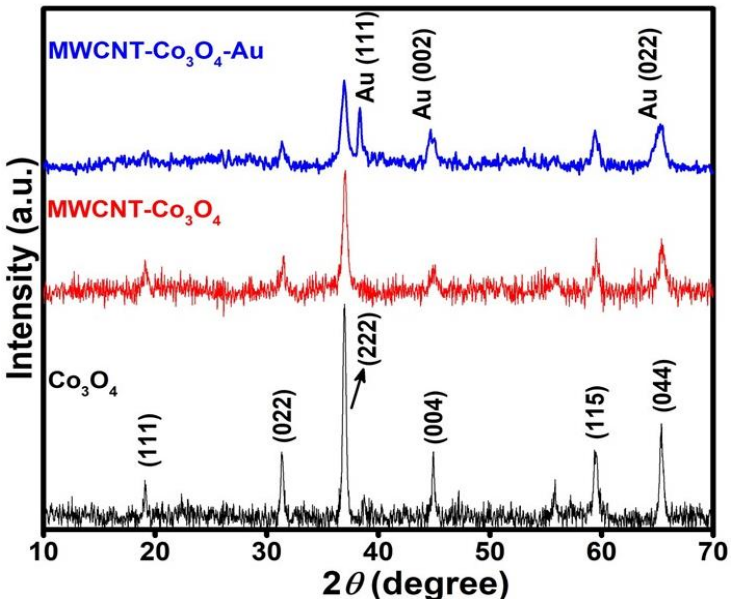

Figure 7: XRD pattern of the Co_3O_4, Co_3O_4@MWCNTs binary and Co_3O_4/Au@MWCNTs ternary composites scanned in the 2θ range of 10°-70°.

3.2.3 XPS analysis of the Co_3O_4/Au@MWCNTs ternary composite

The surface composition and elemental chemical states of the Co_3O_4/Au@MWCNTs ternary composite material were analyzed by XPS as shown in **Figure 8**. The two peaks appeared at about 84.35 and 88.06 eV are attributed to the $4f_{7/2}$ and $4f_{5/2}$, respectively, of the typical metallic Au (**Figure 8a**). [28-30] The O 1s spectrum (**Figure 8b**) exhibits a strong peak at ~529.98 eV and a relatively low intensity peak at ~531.47eV that indicates the presence of at least two kinds of O chemical states; the crystal lattice oxygen (O_L) and hydroxyl oxygen (O_H).[31, 32] A third, relatively low intensity peak at 533.43eV is ascribed to the C-O bond and indicates the direct bonding of oxygen and carbon atoms.[33] The curve fitted C 1s spectrum is shown in **Figure 8c**. The main peak at 284.75 eV is attributed to the sp^2 C–C and the other two peaks are ascribed to the sp^3 C–C and the carbonyl C (C=O) at ~285.83 eV and 288.88eV, respectively.[34-38] Curve fitting for Co core-level spectrum shows the characteristic peaks of Co $2p_{3/2}$ at and Co $2p_{1/2}$ at 779.97 eV and 795.95 eV, with two shake-up satellite peaks, which represents the typical peak formation for Co_3O_4 phase.[39-41]

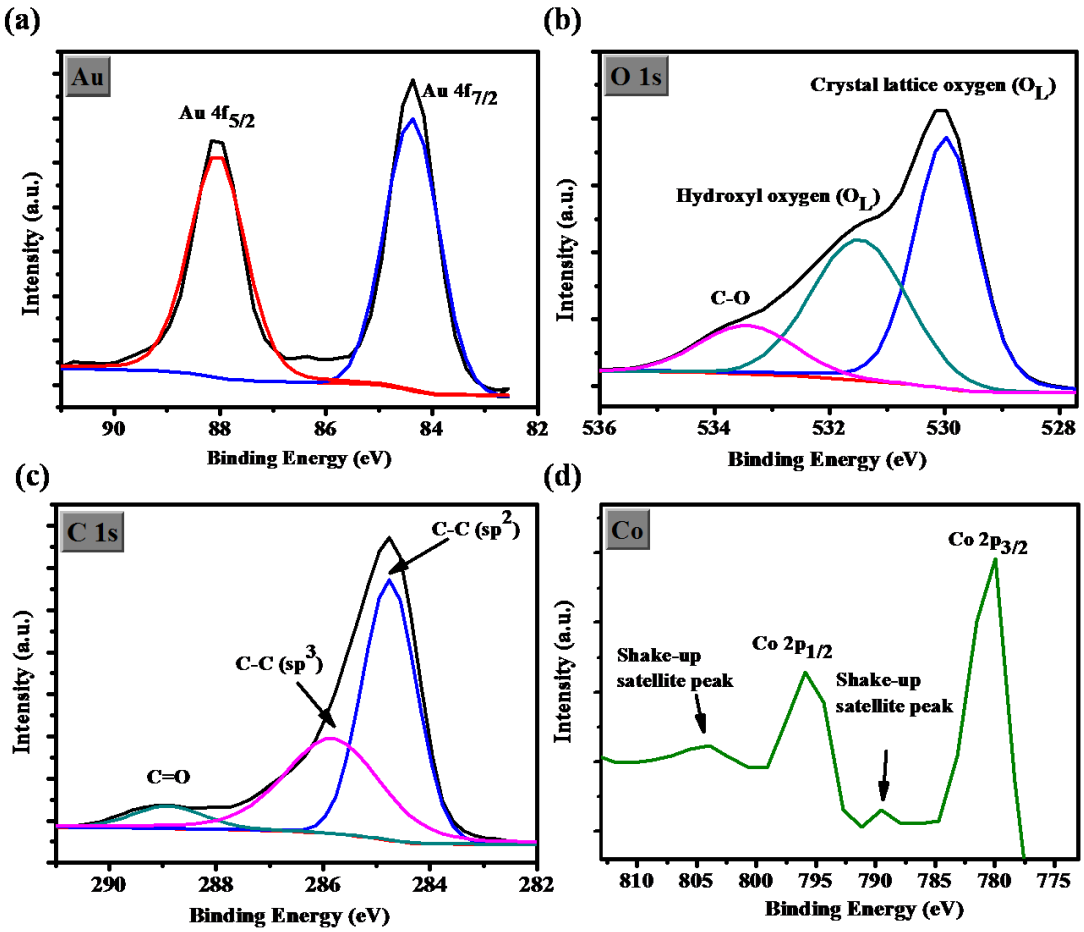

Figure 8: Core-level XPS spectra of the Co_3O_4/Au@MWCNTs ternary composite electrode: **(a)** Au 4f, **(b)** O 1s, **(c)** C 1s and **(d)** Co 2p.

3.3 Electrochemical Analysis

3.3.1 Electrochemical studies of Co_3O_4, Co_3O_4@MWCNTs and Co_3O_4/Au@MWCNTs

The electrochemical studies of the modified electrode were conducted in a standard three-electrode cell system at diverse scanning rates up to 50 mV s^{-1} in 1 M KOH aqueous electrolyte in a potential window of 0.0– 0.5 V (vs. Ag/AgCl). The performance was evaluated on the basis of the capacity difference of the Co_3O_4, its Co_3O_4@MWCNTs binary and Co_3O_4/Au@MWCNTs ternary composite variants as shown in **Figure 9(a-c)**, respectively. It is observed that the increase

in the voltammetric currents is in direct proportion to the scan rates. The typical CV curves of the unaided Co_3O_4 consist of the strong redox peaks that shift towards higher (anodic peaks) and lower (cathodic peaks) potentials at the higher scan rates. The polarization and potential kinetic irreversibility of electrolyte ions access to the electrode interface is responsible for the observed peak potential shift. There is a linear increase in the peak potential with the varied scan rates indicating the good reversibility.[31] The well-defined pair of Co_3O_4 redox peaks exhibit the properties of typical faradaic behavior of a battery-type electrode. However, the battery-type materials based on metal oxides should not be confused with the pseudo-capacitivity of the materials, because the electrochemical signature of battery type and pseudo-capacitive material is different.[27] It is noteworthy that the redox peaks come from the reversibility of cobalt ions transitions with the hydroxyl ion (OH^-) of the alkaline media. Moreover, **Figure 9c** illustrates that the composition of Co_3O_4/Au@MWCNTs ternary composite did not significantly distort the CV curves, ultimately, no pronounced shift was observed in the redox peaks compared to the individual Co_3O_4 or Co_3O_4@MWCNTs binary composite. This phenomenon is associated with the good reversibility behavior of the ternary composite. In addition, a significant increase in the intensity of the Co_3O_4/Au@MWCNTs redox peaks is attributed to the increased conductivity of Au NPs enriched with the extended electron transfer channels during the oxidation and reduction process. This fact implies that synergy of Au NPs in the ternary composite and its decoration on the MWCNTs matrix can definitely improve the electrochemical functioning of the resultant device owing to the enhanced conductivity and capacity fading of the ternary composite.[42] **Figure 9d** compares the performance of individual Co_3O_4, its Co_3O_4@MWCNTs binary and Co_3O_4/Au@MWCNTs ternary composites at a scan rate of 3 mV s^{-1}. Moreover, the

Co_3O_4/Au@MWCNTs ternary composite, due to the high conductivity of MWCNTs matrix and Au NPs, exhibits relatively high background current compared to pristine Co_3O_4 NPs.

The reactions mechanism in 1 M KOH is based on the following **equations**.

$$Co_3O_4 + OH^- + H_2O \leftrightarrow 3CoOOH + e^- \quad \textbf{(1)}$$

It is noteworthy that the CV curves do not display the distinguished pseudocapacitive behavior (rectangular CV curve), that is "steady change of capacitance over the entire potential window", which is coherent with the formerly published findings that describe the electrochemical performance in terms of specific capacity contrary to the specific capacitance.[32] The specific capacity values of all the materials can be computed according to **equation (2):**

$$Qs = \frac{1}{vm}\int_{vi}^{vf} I \times VdV \quad \textbf{(2)}$$

where, the specific capacity is presented by Qs (C/g), scanning rate by v (V/s), active material mass loading by m(g) and the integral part of the equation represents the area under the peak (anodic) of the CV curve. The Co_3O_4/Au@MWCNTs ternary composite showed the highest specific capacity of 108.80 C g^{-1} compared to Co_3O_4@MWCNTs binary composite (57.00 C g^{-1}) and Co_3O_4 (40.90 C g^{-1}) single material.

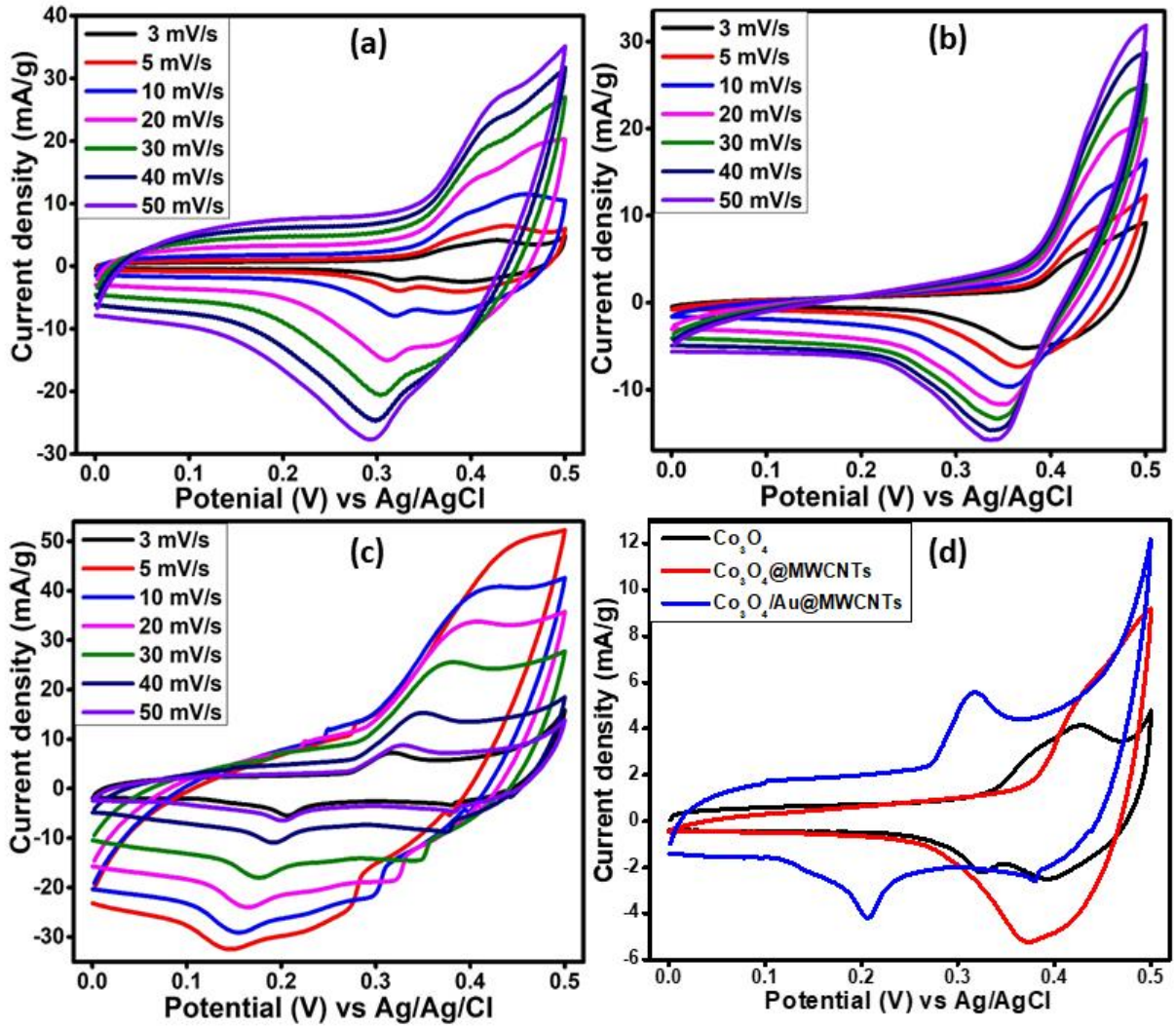

Figure 9: CV curves of **(a)** pristine Co_3O_4NPs **(b)** Co_3O_4@MWCNTs binary and **(c)** Co_3O_4/Au@MWCNTs ternary composite measured at varied scan rates. **(d)** CV curves to compare the electrochemical performance of Co_3O_4 NPs, Co_3O_4@MWCNTs binary and Co_3O_4/Au@MWCNTs ternary composites recorded at 3 mV s^{-1}.

3.3.2 GCD and EIS studies

The GCD curves were recorded to evaluate the capacity performance of the Co_3O_4 and its composite in a potential range of 0-0.5 V at varied current densities (0.1-1.0 A g^{-1}), as presented

in **Figure 10**. The non-linearity of the curves is associated with the faradic behavior which is showing the battery type characteristics of the electrodes. Taking into account, the charge-discharge curves of all three materials, ternary composite (Co_3O_4/Au@MWCNTs) possesses the longest discharge time and hence depicts the best performing electrode material compared to its counterpart electrodes.

The specific capacity (Qs) values of the modified electrodes can be determined from the discharge trends by exploiting the **equation (3)**.

$$Qs = \frac{I \times \Delta t}{m} \qquad \textbf{(3)}$$

where, I(A) is the discharge current, Δt(s) time to fully discharge and m(g) represents the mass loading of the material. The computed specific capacities are 109.77, 57.17 and 41.30 C g^{-1} forCo_3O_4/Au@MWCNTs, Co_3O_4@MWCNTs and Co_3O_4, respectively at a current density of 0.6 A g^{-1}. **Figure 11a** exhibits the specific capacity of all three variants of electrode materials at different scan rates. The $Q_s$values experienced a gradual decay at increased scan rates due to the unsynchronized movement of charges at the corresponding current densities. Moreover, the diffusion or migration of electrolyte ions demonstrates slow diffusion or migration through the electrodes at higher scan rates.[43] The Q_s values were decreased to 12.38, 23.71 and 33.42 C g^{-1} for Co_3O_4, Co_3O_4@MWCNTs binary and Co_3O_4/Au@MWCNTs ternary electrodes, respectively at high scan rates. These values clearly indicate the performance limitation of Co_3O_4 as standalone electrode materials compared to their binary and ternary composites. Significantly improved performance of the binary and ternary composites is attributed to the ability of MWCNTs to disaggregate Co_3O_4 NPs and enhanced conductivity due to the inclusion of highly conductive Au NPs. However, MWCNTs have increased the rate capability, probably due to disaggregation and

random growth of Co_3O_4 NPs on the MWCNTs matrix. It is thus clear from the results illustrated in **Figure 11a** that hybridization of MWCNTs and Au along with the Co_3O_4 base-material has remarkably improved the electrochemical performance of the ternary composite.

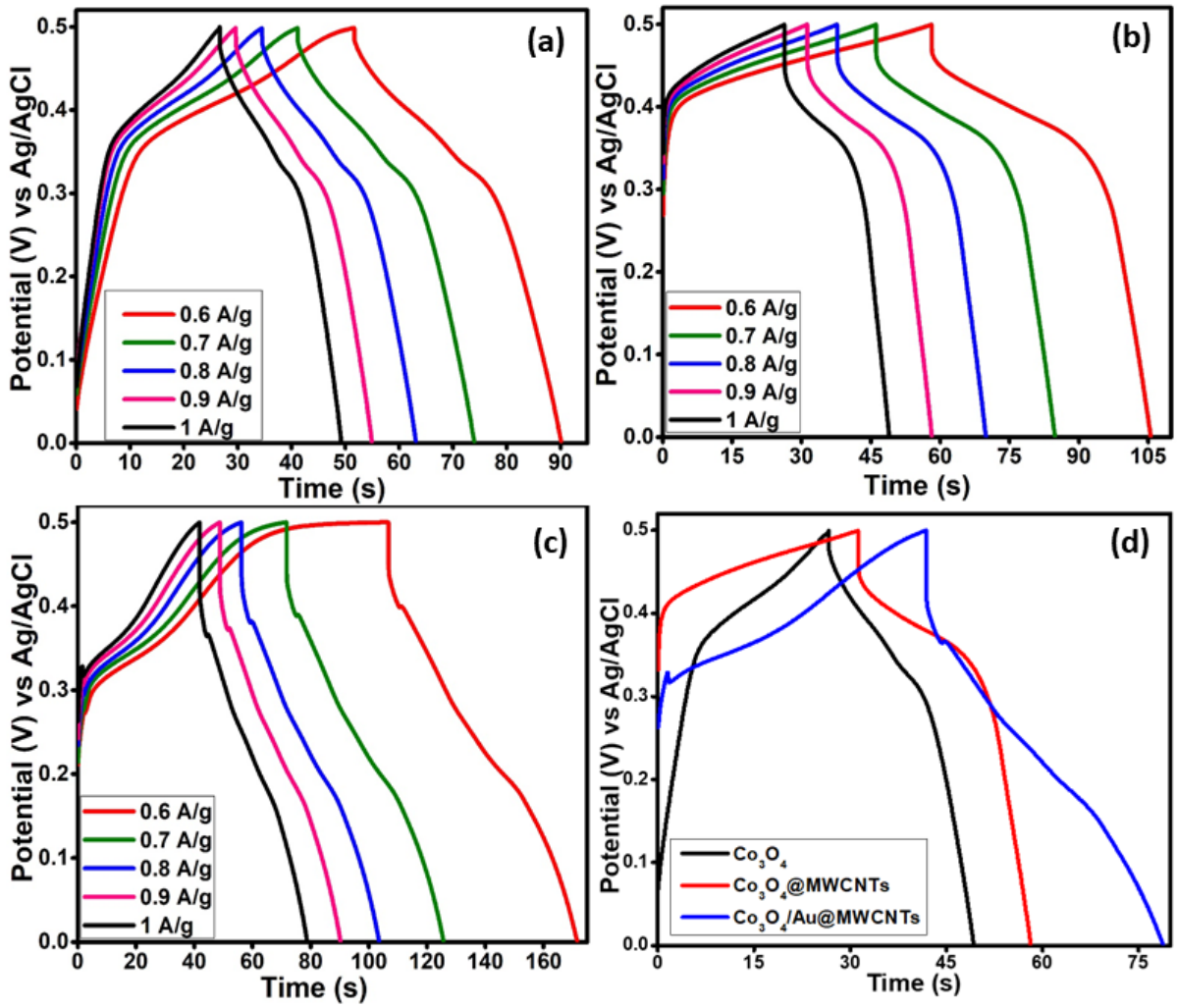

Figure 10: GCD cures at various current densities, **(a)** Co_3O_4, **(b)** Co_3O_4/@MWCNTs, **(c)** Co_3O_4/Au@MWCNTs and **(d)** comparison curves for all three variants at a current density of 0.9 Ag^{-1}.

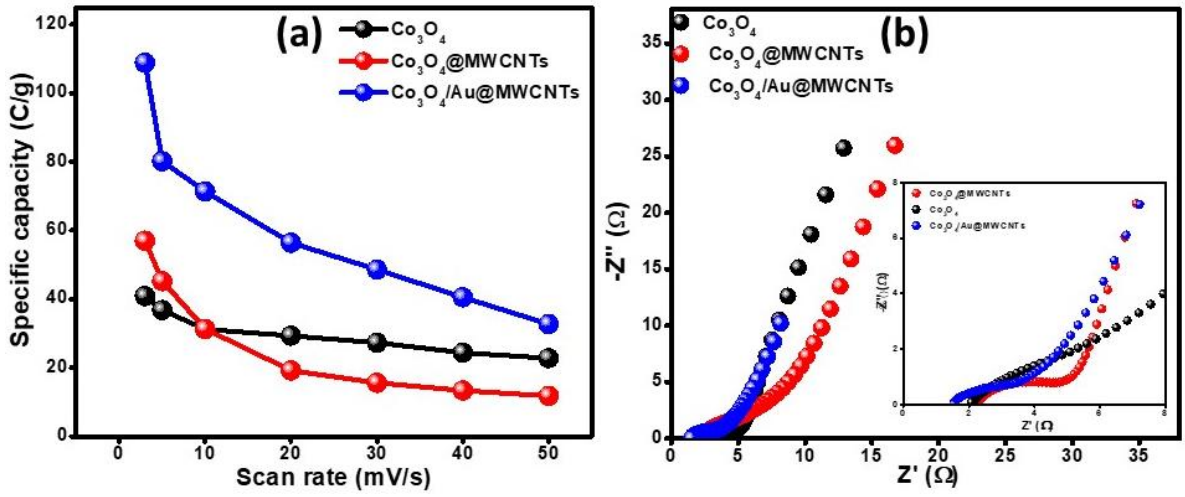

Figure 11: (a) Specific capacities of Co_3O_4 NPs, Co_3O_4@MWCNTs binary and Co_3O_4/Au@MWCNTs ternary composites at various scanning rates. **(b)** Nyquist plots of the Co_3O_4 NPs, Co_3O_4@MWCNTs binary and Co_3O_4/Au@MWCNTs ternary composites. Inset Figure 11(b) shows the EIS spectrum in high frequency region.

The EIS studies are highly regarded as the principal method to evaluate the fundamental behavior of the electrochemical storage devices, particularly, intrinsic mechanism of the electrodes.[44, 45] The Nyquist spectra for Co_3O_4 as well as its binary and ternary variant electrodes are shown in **Figure 11b**. The spectra exhibit a straight line in the low frequency and a semi-circle in the high frequency region. The nearly vertical line in the low frequency region corresponding to the Co_3O_4/Au@MWCNTs ternary composite suggests the nearly ideal capacitive behavior of a supercapacitor with low R_{ct} values. A line parallel to the y-axis ascribes the increased charge storage capability of the Co_3O_4/Au@MWCNTs ternary composite which is obviously expected. The hybridization of MWCNTs and Au along with Co_3O_4 NPs has ultimately enhanced the conductivity of the resultant composite. In addition, the Co_3O_4 exhibited the largest semi-circle

than its binary and ternary variants that indicates its relatively higher charge transfer resistance. It is noteworthy that the agglomeration of Co_3O_4 induces the higher diffusion resistance compared to its variants. Furthermore, the aggregation of Co_3O_4 induces the low specific capacity owing to the agglomeration induced less EC active sites. Contrary to this, the Co_3O_4 NPs form nodes onto the MWCNTs matrix that ultimately provides the large accessible electroactive sites for the Au NPs. Thus, the redox active sites can be increased to carry out electrochemical activity more efficiently. Moreover, the MWCNTs, Co_3O_4, and Au which are in very low dimensions are able to squeeze the path traced for the electronic insertion/disinsertion to the Ni-foam, resulting in the highest retention when equated to unaided Co_3O_4 and Co_3O_4@MWCNTs composite.

4.0 Electrochemical studies of the assembled supercapattery

The EC evaluation of the electrode materials is generally performed in two and three electrodes configurations. The two electrodes configuration is believed to possess relatively closer approach to the real application of electrochemical storage device.[46, 47] Therefore, the supercapattery was assembled in the two electrodes configuration using the best performing electrode material *e.g.* the Co_3O_4/Au@MWCNTs ternary composite, in order to further evaluate the performance. Before assembling the two electrodes configuration, individual CV curves for positive (Co_3O_4/Au@MWCNTs) and negative (AC) electrodes were obtained in the three cells configuration to estimate the maximum stable working potential window as shown in **Figure 12a**. It is evident from the results that the potential range can be extended up to 1.5 V, by combining the 0 to 0.5 V for Co_3O_4/Au@MWCNTs and -1 to 0 V for AC. **Figure 12b** depicts CV curves of an optimized Co_3O_4/Au@MWCNTs ternary composite in two electrodes configuration at varied scan rates from 3 to 100 mV s^{-1}. Nearly rectangular curves with no prominent peak until 0.5 V clearly indicate the EDLC effect which specifies that energy storage occurred due to the

intercalation of OH^- ions at the electrode interface. Moreover, energy storage was induced by faradaic reactions after 0.5 V as the oxidation-reductions peaks also emerged in the mechanism. It can be seen that the curve started to distort beyond 1.5 V and climbed upwards along the vertical axis, which indicates the maximum limit of the potential range. Initially, almost rectangular CV curve indicates the ideal capacitive behavior that is attributed to the AC followed by the wide redox peaks arise from Co_3O_4/Au@MWCNTs composite. Moreover, the amplified intensity of the redox peaks at a higher scan rate and the conserved CV curves clearly indicate the efficacy of the material in terms of stability and rate capability of the resultant device even at higher scan rates, *i.e.*, 100 mV s^{-1}.[48]

The GCD curves of the best performing electrode material (Co_3O_4/Au@MWCNTs ternary composite) based on the two electrodes configuration were obtained at low and high current densities as shown in **Figure 12c and 12d**, respectively at 0.4, 0.5, 0.6, 0.7, 0.8, 0.9 1.0, 1.5, 2.0, 2.5 3.0, 3.5 and 4.0 A g^{-1}. The charge-discharge behavior indicates that the redox process dominates up to the maximum potential window. The typical symmetric GCD curves at varied current densities demonstrated that the devices possess excellent capacitive behavior with prominent reversible redox mechanism.

The power density, *(P)* and energy density, *(E)* values are derived using the **relations (4)** and **(5).**

$$E(Wh/kg) = \frac{\Delta V \times Qs}{2 \times 3.6} \qquad \textbf{(4)}$$

$$P(W/kg) = \frac{E \times 3600}{\Delta t} \qquad \textbf{(5)}$$

where, ΔV, Qs and Δt(s) denote the potential window, the specific capacity (Cg^{-1}) and the discharge time, respectively. The ternary composite based device possesses an energy density, E= 18.80 Wh Kg^{-1} and power density of 302.00 W Kg^{-1} at 0.4 A g^{-1} current density. However, the

significant increase in the power density up to 2577.60 W Kg^{-1} lowered the *E* value to 9.94 Wh Kg^{-1} when current density was increased to 4.0 A g^{-1}.

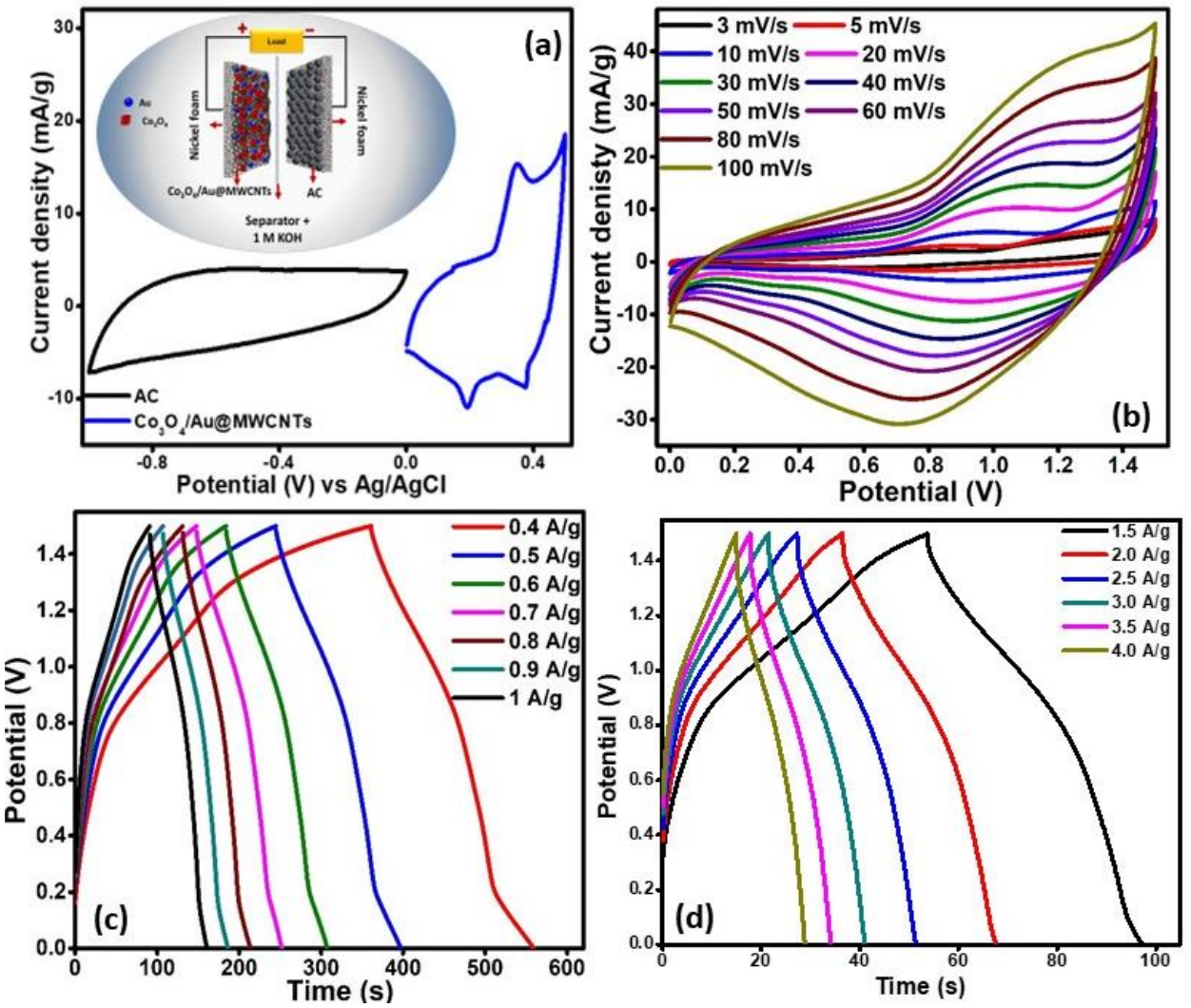

Figure 12: (a) Comparative CV curves of Co_3O_4/Au@MWCNTs ternary composites and AC electrodes performed in a two-electrode cell in KOH aqueous solution at a scan rate of 10 mV s^{-1}. **(b)** CV of optimized Co_3O_4/Au@MWCNTs ternary composites based supercapattery measured at different potential windows. Galvanostatic charge-discharge curves of Co_3O_4/Au@MWCNTs ternary composites supercapattery devices at **(c)** low and **(d)** high current densities.

Figure 13a shows the Nyquist plot of the assembled supercapattery incorporating Co_3O_4/Au@MWCNTs ternary composite as a positive electrode material. As expected, a small semicircle is observed in the high frequency region showing the low charge transfer resistance and the almost vertical line parallel to the imaginary axis demonstrates the high charge storage capability of the device. A good cycle life is a fundamental requirement for a supercapattery device. The cycle life test was carried out for the Co_3O_4/Au@MWCNTs//AC supercapattery over 3500 cycles by charging and discharging at a current density of 4 Ag^{-1} between 0 and 1.5 V. The device showed outstanding electrochemical stability and experienced only 8.30 % deterioration in the initial capacity after 3500 cycles. Therefore, the retention of 91.70 % after 3500 cycles (**Figure 12b)** for the Co_3O_4/Au@MWCNTs//AC supercapattery is promising for its further realization in practical applications.

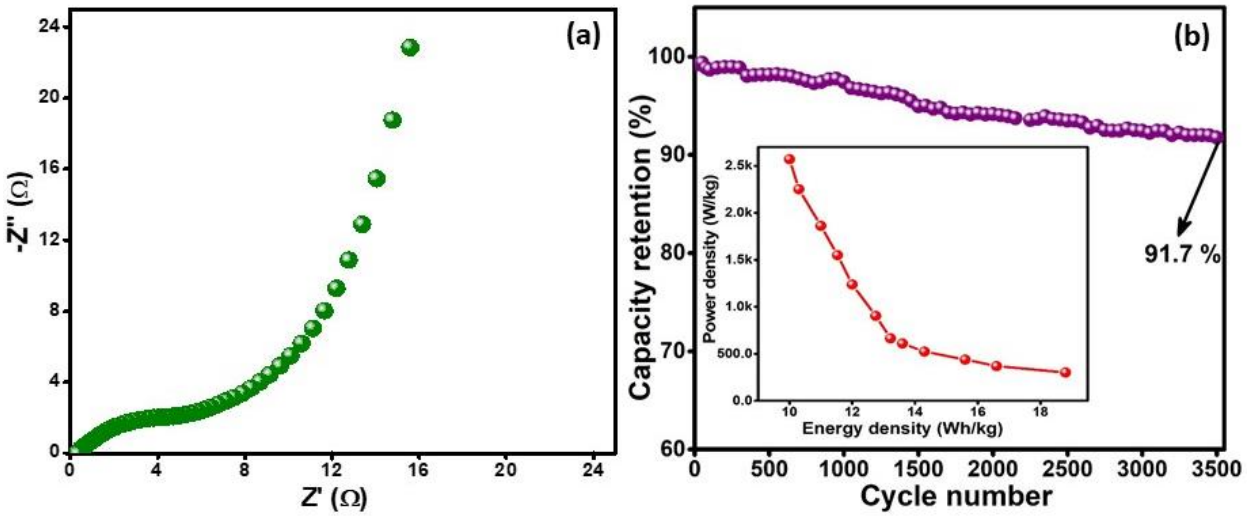

Figure 13: (a) Nyquist plot of Co_3O_4/Au@MWCNTs ternary composite in the assembled device. **(b)** Cycle performance of the Co_3O_4/Au@MWCNTs ternary composite electrode as a function of the number of cycles at a current density of 4 A g^{-1} in 1 M KOH. The inset shows the power density decay vs energy density of the assembled devices.

5. CONCLUSIONS

In summary, a novel supercapattery based on Co_3O_4/Au@MWCNTs ternary composite as a positive electrode and AC as a negative electrode, has been assembled in a 1 M KOH electrolyte. The as-prepared composite of Co_3O_4 and Au NPs decorated on MWCNTs to form ternary composite potentially possessed enhanced electroactive sites and conductivity due to disaggregation of Co_3O_4 NPs and highly conductive Au NPs. The disaggregation drawback of Co_3O_4 NPs has also been modeled using DFT simulation. The ternary composite was cycled reversibly in a stable potential region of 0-1.5 V that demonstrated the enhanced energy density of 18.80 Wh Kg^{-1} and a corresponding power density 302.00 W Kg^{-1} at a current density of 0.4 A g^{-1}. More importantly, the ternary composite prevents the degradation of the resultant electrode during cyclic lifetime, resulting in a promising cycle life with a retention value of 91.70 % even after 3500 reversible cycles. Therefore, the newly synthesized Co_3O_4/Au@MWCNTs ternary composite in the present study can be regarded as a promising candidate for its exploitation in high performing energy storage devices possessing high energy density, longer cyclic life and excellent rate capability.

ACKNOWLEDGMENTS

The financial support provided by the University of Malaya (Grant UMRG: RG382-17AFR). We would also like to thank the Solar Photovoltaic Academic Research Consortium II (SPARC II) project, funded by the WEFO (Welsh European Funding Office) for support.

REFERENCES

1. M. Salanne, B. Rotenberg, K. Naoi, K. Kaneko, P.-L. Taberna, C. P. Grey, B. Dunn and P. Simon, *Nature Energy*, 2016, **1**, 16070.

2. J. Y. Hwang, M. Li, M. F. El-Kady and R. B. Kaner, *Advanced Functional Materials*, 2017, **27**, 1605745.

3. K.-J. Huang, J.-Z. Zhang and J.-L. Cai, *Electrochimica Acta*, 2015, **180**, 770-777.

4. C. He, Y. Liang, P. Gao, L. Cheng, D. Shi, X. Xie, R. K.-Y. Li and Y. Yang, *Composites Part B: Engineering*, 2017, **121**, 68-74.

5. J. Yan, Q. Wang, T. Wei and Z. Fan, *Advanced Energy Materials*, 2014, **4**.

6. W. Liu, C. Lu, H. Li, R. Y. Tay, L. Sun, X. Wang, W. L. Chow, X. Wang, B. K. Tay and Z. Chen, *Journal of Materials Chemistry A*, 2016, **4**, 3754-3764.

7. G. Cai, P. Darmawan, M. Cui, J. Wang, J. Chen, S. Magdassi and P. S. Lee, *Advanced Energy Materials*, 2016, **6**, 1501882.

8. B. K. Kim, S. Sy, A. Yu and J. Zhang, *Handbook of Clean Energy Systems*, 2015, 1-25.

9. T. Cheng, Y.-Z. Zhang, J.-D. Zhang, W.-Y. Lai and W. Huang, *Journal of Materials Chemistry A*, 2016, **4**, 10493-10499.

10. W.-J. Zhang and K.-J. Huang, *Inorganic Chemistry Frontiers*, 2017, **4**, 1602-1620.

11. J. R. Miller and P. Simon, *Science Magazine*, 2008, **321**, 651-652.

12. M. Winter and R. J. Brodd, *Journal*, 2004.

13. J. Iqbal, A. Numan, S. Rafique, R. Jafer, S. Mohamad, K. Ramesh and S. Ramesh, *Electrochimica Acta*, 2018, **278**, 72-82.

14. H. Shao, N. Padmanathan, D. McNulty, C. O′ Dwyer and K. M. Razeeb, *ACS applied materials & interfaces*, 2016, **8**, 28592-28598.

15. D. He, G. Liu, A. Pang, Y. Jiang, H. Suo and C. Zhao, *Dalton Transactions*, 2017, **46**, 1857-1863.

16. E. Iwama, K. Kisu, W. Naoi, P. Simon and K. Naoi, in *Metal Oxides in Supercapacitors*, Elsevier, 2017, pp. 247-264.

17. L.-L. Xing, G.-G. Zhao, K.-J. Huang and X. Wu, *Dalton transactions*, 2018, **47**, 2256-2265.

18. M.-J. Deng, F.-L. Huang, I.-W. Sun, W.-T. Tsai and J.-K. Chang, *Nanotechnology*, 2009, **20**, 175602.

19. A. Numan, M. M. Shahid, F. S. Omar, K. Ramesh and S. Ramesh, *Sensors and Actuators B: Chemical*, 2017, **238**, 1043-1051.

20. Z. Fang, W. Xu, T. Huang, M. Li, W. Wang, Y. Liu, C. Mao, F. Meng, M. Wang and M. Cheng, *Materials Research Bulletin*, 2013, **48**, 4419-4423.

21. C. Wu, Q. Shen, R. Mi, S. Deng, Y. Shu, H. Wang, J. Liu and H. Yan, *Journal of Materials Chemistry A*, 2014, **2**, 15987-15994.

22. L.-L. Xing, X. Wu and K.-J. Huang, *Journal of colloid and interface science*, 2018, **529**, 171-179.

23. M. M. Shahid, A. H. Ismail, A. M. A. A. AL-Mokaram, R. Vikneswaran, S. Ahmad, A. Hamza and A. Numan, *Progress in Natural Science: Materials International*, 2017, **27**, 582-587.

24. V. N. Popov, *Materials Science and Engineering: R: Reports*, 2004, **43**, 61-102.

25. K. I. Ozoemena and S. Chen, *Nanomaterials in advanced batteries and supercapacitors*, Springer, 2016.

26. G. Pandey and S. Hashmi, *Journal of Power Sources*, 2013, **243**, 211-218.

27. D. P. Dubal, O. Ayyad, V. Ruiz and P. Gomez-Romero, *Chemical Society Reviews*, 2015, **44**, 1777-1790.

28. C. Shan, F. Li, F. Yuan, G. Yang, L. Niu and Q. Zhang, *Nanotechnology*, 2008, **19**, 285601.

29. M. K. Bayazit, S. A. Hodge, A. J. Clancy, R. Menzel, S. Chen and M. S. Shaffer, *Chemical Communications*, 2016, **52**, 1934-1937.

30. R. A. Smith, *Platinum Metals Review*, 2009, **53**, 109-110.

31. F. Cui, L. Xu, T. Cui, T. Yao, J. Yu, X. Zhang and K. Sun, *RSC Advances*, 2014, **4**, 33408-33415.

32. G. Ai, R. Mo, H. Li and J. Zhong, *Nanoscale*, 2015, **7**, 6722-6728.

33. S. Rafique, S. M. Abdullah, K. Sulaiman and M. Iwamoto, *Organic Electronics*, 2017, **40**, 65-74.

34. M. Seredych, A. V. Tamashausky and T. J. Bandosz, *Advanced Functional Materials*, 2010, **20**, 1670-1679.

35. C. Mattevi, G. Eda, S. Agnoli, S. Miller, K. A. Mkhoyan, O. Celik, D. Mastrogiovanni, G. Granozzi, E. Garfunkel and M. Chhowalla, *Advanced Functional Materials*, 2009, **19**, 2577-2583.

36. P. Han, Y. Yue, Z. Liu, W. Xu, L. Zhang, H. Xu, S. Dong and G. Cui, *Energy & Environmental Science*, 2011, **4**, 4710-4717.

37. Y.-J. Noh, S.-C. Park, I.-T. Hwang, J.-H. Choi, S.-S. Kim, C.-H. Jung and S.-I. Na, *Carbon*, 2014, **79**, 321-329.

38. S. Rafique, S. M. Abdullah, J. Iqbal, A. Jilani, S. Vattamkandathil and M. Iwamoto, *Organic Electronics*, 2018, **59**, 140-148.

39. S. Huang, Y. Jin and M. Jia, *Electrochimica Acta*, 2013, **95**, 139-145.

40. C. Feng, J. Zhang, Y. He, C. Zhong, W. Hu, L. Liu and Y. Deng, *ACS nano*, 2015, **9**, 1730-1739.

41. M. Qorbani, N. Naseri and A. Z. Moshfegh, *ACS applied materials & interfaces*, 2015, **7**, 11172-11179.

42. H. Xia, C. Hong, X. Shi, B. Li, G. Yuan, Q. Yao and J. Xie, *Journal of Materials Chemistry A*, 2015, **3**, 1216-1221.

43. Q. Fu, F. Tietz and D. Stöver, *Journal of The Electrochemical Society*, 2006, **153**, D74-D83.

44. Z. Fan, J. Yan, T. Wei, L. Zhi, G. Ning, T. Li and F. Wei, *Advanced Functional Materials*, 2011, **21**, 2366-2375.

45. W. Sugimoto, H. Iwata, K. Yokoshima, Y. Murakami and Y. Takasu, *The Journal of Physical Chemistry B*, 2005, **109**, 7330-7338.

46. X. Zhang, J. Wang, J. Liu, J. Wu, H. Chen and H. Bi, *Carbon*, 2017, **115**, 134-146.

47. Y. Li, G. Louarn, P.-H. Aubert, V. Alain-Rizzo, L. Galmiche, P. Audebert and F. Miomandre, *Carbon*, 2016, **105**, 510-520.

48. Q. Wang, D. Chen and D. Zhang, *RSC Advances*, 2015, **5**, 96448-96454.